JGR Atmospheres

RESEARCH ARTICLE
10.1029/2023JD038616

Key Points:

- Responses in the South Asian High (SAH) show consistent patterns at 100 hPa in the periods of increased and stabilizing radiative forcing
- Opposite changes in the SAH at different altitudes are mainly due to the maximum potential temperature at 150–200 hPa
- The mean advection of stratification and apparent heat changes are crucial to the SAH responses

Supporting Information:

Supporting Information may be found in the online version of this article.

Correspondence to:

X. Qu and G. Huang,
quxia@mail.iap.ac.cn;
hg@mail.iap.ac.cn

Citation:

Hou, H., Qu, X., & Huang, G. (2023). Persistently southward of the South Asian high during the radiative forcing stabilization. *Journal of Geophysical Research: Atmospheres*, *128*, e2023JD038616. https://doi.org/10.1029/2023JD038616

Received 25 FEB 2023
Accepted 4 AUG 2023

Author Contributions:

Conceptualization: Xia Qu, Gang Huang
Data curation: Hongyu Hou
Formal analysis: Hongyu Hou
Funding acquisition: Xia Qu, Gang Huang
Investigation: Hongyu Hou
Methodology: Xia Qu, Gang Huang
Project Administration: Xia Qu, Gang Huang
Software: Hongyu Hou, Xia Qu
Supervision: Xia Qu, Gang Huang
Validation: Hongyu Hou
Visualization: Hongyu Hou, Xia Qu, Gang Huang
Writing – original draft: Hongyu Hou
Writing – review & editing: Hongyu Hou, Xia Qu, Gang Huang

Persistently Southward of the South Asian High During the Radiative Forcing Stabilization

Hongyu Hou[1,2], Xia Qu[1,3], and Gang Huang[1,2,4]

[1]State Key Laboratory of Numerical Modeling for Atmospheric Sciences and Geophysical Fluid Dynamics, Institute of Atmospheric Physics, Chinese Academy of Sciences, Beijing, China, [2]University of Chinese Academy of Sciences, Beijing, China, [3]Center for Monsoon System Research, Institute of Atmospheric Physics, Chinese Academy of Sciences, Beijing, China, [4]Laboratory for Regional Oceanography and Numerical Modeling, Qingdao National Laboratory for Marine Science and Technology, Qingdao, China

Abstract The South Asian high (SAH), a large-scale anticyclone at 100 and 200 hPa on the Asian continent, is driven by South Asian summer monsoon rainfall and heating over the Tibetan Plateau. As one member of the Asian summer monsoon system, the changes of its location and intensity may cause other climate responses. Rainfall-induced latent heating can affect the SAH change. Previous study revealed that rainfall responses in Indian Ocean are opposite in periods of increased and stabilizing radiative forcing (RF) due to the deep ocean warming over the Southern Ocean. SAH responses during RF increase and stabilization are studied with 13 models from the Extended Representative Concentration Pathway scenario 4.5 (ECP4.5) experiment. At 100 hPa, the SAH intensifies and moves equatorward in increased RF scenario; when RF stabilizing, SAH still shifts southward but with little change in intensity. At 200 hPa, the SAH changes little in both RF increase and stabilization. These opposite responses at different altitudes may be due to the maximum potential temperature at 150–200 hPa, leading to the opposite changes in vertical motion. Results of the linear baroclinic model indicate that (a) during RF increase, diabatic heating (Q_1^*) contributes to SAH strengthening, both Q_1^* and the mean advection of stratification change (*MASC*) lead to SAH southward movement; (b) during RF stabilization, Q_1^* and *MASC*, contribute to the SAH equatorward displacement. Two components of Q_1^*, the latent heating and residual heating, are canceled out and lead to little change in SAH intensity.

Plain Language Summary To mitigate global warming, the 2015 Paris Agreement set out a goal that the global mean surface temperature should be confined to rise to 1.5°C above preindustrial level. This goal requires radiative forcing (RF) to stabilize or decrease. Our previous study revealed that rainfall changes in Indian Ocean display opposite patterns in periods of increased and stabilizing RF. Rainfall-induced latent heating may affect the South Asian High (SAH) response. Present research focuses on the SAH responses in increased and stabilizing RF scenario. At 100 hPa, in increased RF, the SAH intensifies and moves equatorward; during RF stabilization, the SAH shifts southward but barely strengthens. At 200 hPa, the SAH responses are inconsistent due to the opposite sign of the vertical temperature advection. The outputs of linear baroclinic model manifested the following: (a) during RF increase, the SAH strengthening is mainly due to diabatic heating (Q_1^*), and its southward shift is due to both Q_1^* and the mean advection of stratification change (*MASC*); (b) during RF stabilization, Q_1^* and *MASC*, lead to the SAH moving equatorward. These findings indicate that the climate responses are different during RF stabilization, which is crucial for the proposal of the 2015 Paris Agreement.

1. Introduction

During summer in Northern Hemisphere, there is a large-scale anticyclone in the upper troposphere and lower stratosphere on the Asian continent. This anticyclone is called the South Asian high (SAH) which is generated by topographic heating and large-scale land–sea warming contrast (Boos & Kuang, 2010; Wu et al., 2012; Zhao et al., 2014). It is the most powerful and stable system in the upper troposphere (Mason & Anderson, 1963). Its closed streamlines can trap interior pollutants that enter through deep convection (Bian et al., 2020). They may remain inside for relatively long periods and are separate from the outside. Subtropical westerly jet on its north is a crucial atmospheric background for forming the East Asia–Meiyu–Baiu rain belt (Sampe & Xie, 2010). Meanwhile, it is also a parclose for air exchange between the SAH interior and midlatitude stratosphere (Bian et al., 2020). The tropical easterly jet on the south flank of SAH may affect the formation of tropical cyclones, weakening easterly shear may be contribute to more tropical storm formation in the north Indian Ocean (IO) during summer monsoon season (Krishna, 2009; Rao et al., 2008). Northerly airflow on the SAH east and beneath, lower southerly winds give an essential background field for tilted Pacific–Japan pattern (PJ pattern; Kosaka & Nakamura, 2006). Strong meridional wind components of the SAH also help to facilitate air exchange between the upper troposphere in the tropics and the lower stratosphere in midlatitude (Bian et al., 2020). In addition, strong upward motion in the SAH center may carry pollutants to the tropopause, and it is a critical pathway for material exchange between the stratosphere and troposphere (Zhang et al., 2021).

Since the mid-nineteenth century, the concentrations of greenhouse gases in the atmosphere have been increasing due to human activities, resulting in a significant increase of global mean surface air temperature (GMST; von Schuckmann et al., 2016; Wang et al., 2020). However, global warming is spatially uneven due to different heat absorptions and distributions of land and ocean (Wei et al., 2019). This may cause an inhomogeneous response in the atmosphere (Xie et al., 2010). To jointly tackle challenge of climate change and mitigate global warming, nearly 200 parties around the world signed the Paris Agreement in 2015. They aim to weaken the global greenhouse gas emissions increase and confine the global temperature rise to 2°C in this century, and working to limit to 1.5°C. The proposal of this warming target requires radiative forcing (RF) to stabilize or decrease (Sanderson et al., 2016). Past researches have pay attention to the climate responses during RF increase, but fewer studies have examined changes during RF stabilization.

During RF increase, the GMST has an immediate response, similar to the RF pathway; however, during RF stabilization, the GMST grows steadily with a slower pace rather than holding steady (Hou et al., 2021; Long et al., 2020). Past researches have indicated that it is due to different contributions between ocean fast and slow responses (Dickinson, 1981; Held et al., 2010). When increased RF, ocean mixed layer absorbs heat and then exchanges energy with the deep ocean and atmosphere (Dickinson, 1981; Long et al., 2018). It is the ocean fast response, which represents a rapidly exchanging energy process in the ocean mixed layer. Oceanic warming gradually transfers heat downward to deep ocean. When the RF stabilizes or decreases, it displays uniform warming above 2,000 m (Long et al., 2014). Continuing deep ocean heat uptake may change oceanic stratification and currents, as well as atmospheric circulation, which is the ocean slow response (Manabe et al., 1990). Throughout the periods of RF increase and stabilization, the ocean fast and slow responses always exist, and relative contribution of the latter may become greater during RF stabilization due to heat accumulation (Long et al., 2018).

Deep ocean warming may affect the atmospheric responses. Previous research has revealed that the rainfall patterns in IO are different in periods of increased and stabilizing RF (Hou et al., 2021): during RF increase, rainfall change displays a northwest-southeast dipole over the IO; when RF stabilizing, it displays a southwest–northeast dipole due to deep ocean warming over the Southern Ocean. Rainfall-induced latent heating affects the SAH response in RF increasing (Qu & Huang, 2016). These various rainfall patterns in RF increasing and stabilizing may also affect changes in the SAH. In addition, Ma et al. (2012) pointed out that the mean advection of stratification change (*MASC*), which reflects the changes in atmospheric stratification, may slowdown the circulation under global warming. Recently, studies have revealed that *MASC* influences atmospheric responses under global warming (Hou et al., 2021; Qu & Huang, 2016). Therefore, how the SAH responds to different RF pathways and the associated mechanisms is the main focus of this study.

The rest in this article is structured as below. Section 2 provides data and methods. Section 3 shows the SAH responses during different RF change scenarios. Section 4 proposes a mechanism to explain the different responses of the SAH. Section 5 provides the model spread of the SAH responses during RF increase and stabilization, and the last section is summary and discussion.

2. Data and Methods

2.1. Data

This research is based on the Coupled Model Intercomparison Project Phase 5 (CMIP5) outputs, monthly results are used which are from the historical and Extended Representative Concentration Pathway scenario 4.5 (ECP4.5) experiments as listed in Table 1. The ECP4.5 output is a subset output extending to 2,300 in the Representative Concentration Pathways 4.5 scenario simulation (RCP4.5). There are 13 models that meet these conditions. Although ECP4.5 is a subset sample of CMIP5 models, Sniderman et al. (2019) pointed out that the ECP subset can represent the full set of CMIP5 models by examining their performances in simulating rainfall changes in the

10.1029/2023JD038616

Table 1
List of Coupled Model Intercomparison Project Phase 5 Models and Their Affiliations

No.	Model name	Affiliation institution
1	bcc-csm1-1	Beijing Climate Center, China Meteorological Administration, China
2	CanESM2	Canadian Center for Climate Modeling and Analysis, Canada
3	CESM1-CAM5	National Center for Atmospheric Research, USA
4	CNRM-CM5	Center National de Recherches Météorologiques, Center Européen de Recherche et de Formation Avancée en Calcul Scientifique, France
5	CSIRO-Mk3.6.0	Commonwealth Scientific and Industrial Research Organization in collaboration with Queensland Climate Change Center of Excellence, Australia
6	FGOALS-s2	LASG, Institute of Atmospheric Physics, China
7	GISS-E2-H	NASA/GISS Goddard Institute for Space Studies, USA
8	GISS-E2-R	
9	IPSL-CM5A-LR	Institute Pierre Simon Laplace, France
10	IPSL-CM5A-MR	
11	MIROC-ESM	Atmosphere and Ocean Research Institute (The University of Tokyo), National Institute for Environmental Studies, and Japan Agency for MIROC5 Marine-Earth Science and Technology, Japan
12	MPI-ESM-LR	Max Planck Institute for Meteorology, Germany
13	NorESM1-M	Norwegian Climate Center, Norway

twenty-first century. The historical experiment is employed by the observed anthropogenic and natural forcing from 1850 to 2005. The RF of the ECP4.5 experiment rises to approximately +4.5 W m^{-2} around 2,100 and then remains stable to 2,300 (Figure 1). Model outputs are interpolated onto 1.0° × 1.0° grids using bilinear interpolation technique. The multimodel ensembles (MME) are convenient for simulating the SAH to reduce the systematic biases and natural variability of the models. The member "r1i1p1" in each model is used. The model outputs from the Coupled Model Intercomparison Project phase 6 (CMIP6) are too few to analyze, only 2 models have uploaded the required data—GISS-E2-1-H and GISS-E2-1-G in SSP2-4.5, whose RF path first increases and then stabilizes; they are also not adaptable to this research.

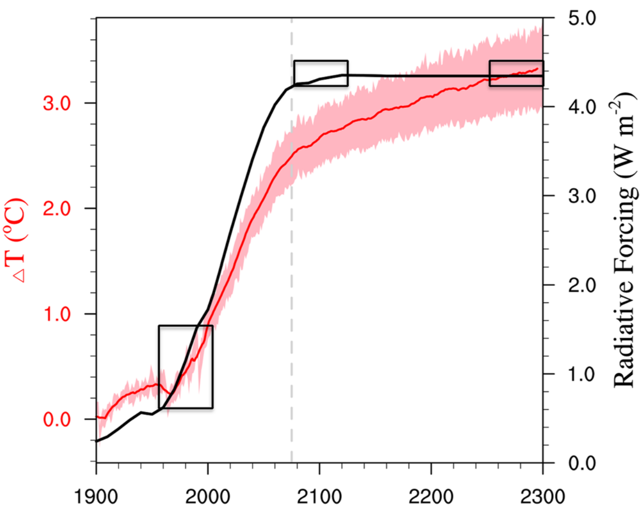

Figure 1. Evolution of the radiative forcing (RF; black line; units: W m^{-2}) and global mean surface air temperature change (GMST, units: °C; red line using 11-year running mean) in boreal summer. GMST is relative to average of 1850–1900 reference. The gray vertical dotted line is the year 2075 which separates periods between increased and stabilizing RF. The pink shading denotes one standard deviation of intermodel variability. Black rectangle boxes represent the three 50-year periods (1956–2005, 2076–2125, and 2251–2300) to define the changes under different RF pathways.

Simulations of the SAH climate state by the CMIP5 models are evaluated based on the National Centers for Environmental Prediction-National Center for Atmosphere Research (NCEP-NCAR) atmospheric reanalysis, whose resolution is 2.5° latitude × 2.5° longitude in the horizontal direction (Kalnay et al., 1996). This research analyzes the mean during summer in Northern Hemisphere (June–August), when the SAH is strongest and most steady. The definition of latitude of the SAH zonal ridge is average latitude of 0 m s^{-1} meridional wind in East Asia region (20–35°N, 20–120°E). The longitude of SAH meridional ridge is average longitude of 0 m s^{-1} zonal wind in the same region.

The year 2075 is chosen to split two responses because it is the turning point of RF (Zheng et al., 2019). The response in increased RF is the anomaly between average of 2076–2125 and average of 1956–2005, and the change during RF stabilizing is the anomaly between average of 2251–2300 and average of 2076–2125. The results are similar if using different period definitions.

2.2. The Simulation of the Linear Baroclinic Model

To test the atmospheric responses to heating, the linear baroclinic model (LBM) is employed in this study (Hou et al., 2021; Ma & Xie, 2013; Qu &

Huang, 2016). The model consists of atmospheric primitive equations, and it can examine linear dynamics in the atmosphere by removing nonlinear process from the model to understand complex atmospheric feedback sequences (Watanabe & Kimoto, 2000). This research uses the "steady forcing" package to analyze the role of heating on the responses. In horizontal direction, its resolution is set to T42 and 20 sigma (σ) in vertical direction. Its climatology uses the summer mean (JJA) of CMIP5 MME of average in 1956–2005 during increased RF and average of 2076–2125 during RF stabilizing. The maximum e-folding decay time for horizontal diffusion is 6 hr. The Rayleigh friction and Newtonian damping time scales are 1 day^{-1} for $\sigma > 0.9$ and $\sigma \leq 0.02$, 5 day^{-1} for $\sigma = 0.9$, and 15 day^{-1} for $\sigma = 0.8$ and 30 day^{-1} for $0.02 < \sigma < 0.8$. The vertical diffusion for all layers is 1,000 day^{-1}. It is integrated of 50 days to get the stable state, and average of the last 20 days are analyzed. Meanwhile, since the forcing during RF stabilizing is too small to offset the internal disturbance of LBM, it is expanded 10 times to approximate the magnitude of forcing during increased RF, and results are reduced by 10, as in methods in Hou et al. (2021).

2.3. Vorticity Equation

The linearized equation of the vorticity budget is (Qu et al., 2022):

$$f\frac{\partial \omega'}{\partial p} - \overline{\vec{V}} \cdot \nabla \zeta' - \vec{V}' \cdot \nabla \overline{\zeta} - \beta v' = 0 \tag{1}$$

the overbar is the climate basic state and prime denotes anomaly in periods of increased and stabilizing RF, respectively. f represents the Coriolis parameter, p denotes pressure, ω denotes pressure velocity, $\vec{V}$ denotes horizontal velocity, ζ denotes relative vorticity, and β represents latitudinal gradient of the Coriolis parameter.

2.4. Thermodynamic Equation Under Global Warming

A regional atmospheric response to an imposed heating distribution under global warming is (Ma et al., 2012; Qu & Huang, 2016):

$$B\left(\overline{\omega}\frac{\partial \theta^*}{\partial p} + \omega'\frac{\partial \overline{\theta}}{\partial p}\right) = -B\overline{\omega}\frac{\partial \langle \theta' \rangle}{\partial p} + LH^* + Re^* \tag{2}$$

where $B = \frac{T}{\theta} = \left(\frac{p}{p_s}\right)^{\frac{R_{dry}}{C_p}}$, p_s represents surface pressure, θ denotes potential temperature, T denotes air temperature, C_p denotes specific heat at constant pressure and R_{dry} denotes gas constant for air. The above equation only considers the vertical motion of diabatic heating because the horizontal motion is smaller than the vertical direction after diagnosis (Ma et al., 2012). At the same time, the local time derivative of temperature is ignored due to analyzing the time mean results. $\langle x \rangle$ represents the global mean, the spatial pattern is $x^* = x' - \langle x' \rangle$. $-B\overline{\omega}\frac{\partial \langle \theta' \rangle}{\partial p}$ is *MASC*. The linearized *LH* response is:

$$LH' = -L\left(\overline{\vec{V}} \cdot \nabla q' + \vec{V}' \cdot \nabla \overline{q} + \overline{\omega}\frac{\partial q'}{\partial p} + \omega'\frac{\partial \overline{q}}{\partial p}\right) \tag{3}$$

q denotes specific humidity, L denotes the latent heat of condensation. The residual terms (*Re*) can be written as:

$$Re' = SH' + Q_R' = Q_1' - LH' \tag{4}$$

where *SH* is sensible heating, Q_R is radiation. The process of concrete derivation in Equation 2 can refer to Ma et al. (2012). The apparent heat source (Q_1; Yanai et al., 1973) is:

$$Q_1' = C_p\left(\overline{\vec{V}} \cdot \nabla T' + \vec{V}' \cdot \nabla \overline{T} + B\overline{\omega}\frac{\partial \theta'}{\partial p} + B\omega'\frac{\partial \overline{\theta}}{\partial p}\right) \tag{5}$$

Additionally, Q_1^* is calculated in this paper to analyze the regional atmospheric response.

2.5. SAH Simulation in CMIP5

First, the performance of SAH simulations in CMIP5 models is first examined by comparing climatology states of the CMIP5 historical experiment with the NCEP-NCAR reanalysis in 1956–2005. Previous studies have used

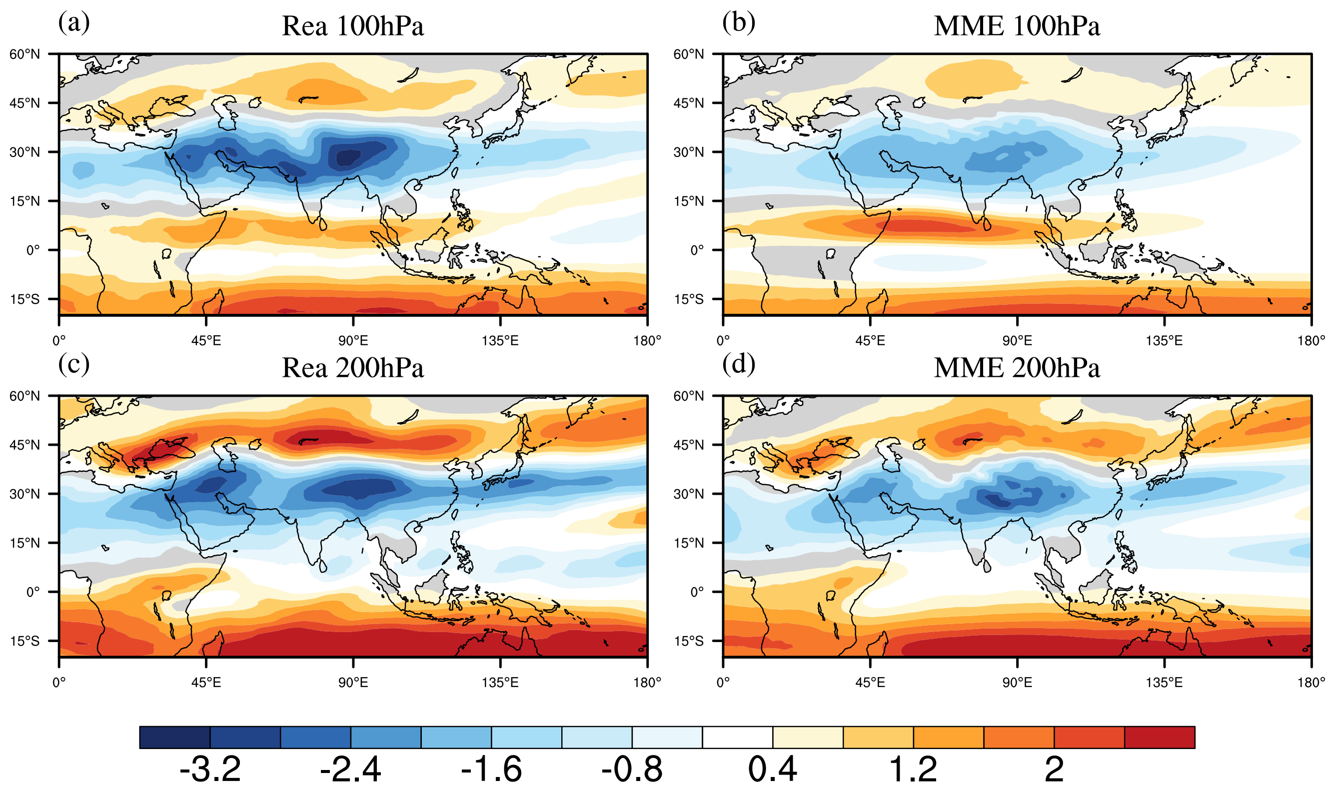

Figure 2. The climatology of vorticity at 100 hPa (a, b) and 200 hPa (c, d) over East Asia (units: $1 \times 10^{-5}\ s^{-1}$; color shading) in 1956–2005. Left panels are the results from the National Centers for Environmental Prediction-National Center for Atmosphere Research (NCEP-NCAR) reanalysis. Right panels show the multimodel ensemble (MME) results in the Coupled Model Intercomparison Project Phase 5 (CMIP5) historical experiment.

geopotential height to represent the SAH, but He et al. (2016) pointed out that under global warming, more than 80% of the geopotential height rise was due to zonal uniform warming. Gradients in geopotential height can cause changes in atmospheric circulation. Therefore, negative vorticity is used to represent the SAH to avoid artificially removing the warming signal.

At 100 hPa, a large negative vorticity exists over East Asia, whose center is located in the region of 15–40°N, 20–120°E from NCEP-NCAR reanalysis results (Figure 2a). The CMIP5 MME can depict these major features, but the amplitude is weaker (Figure 2b). Similar to these results at 100 hPa, the SAH at 200 hPa is an apparent negative value over East Asia (Figure 2c) but flatter and longer. The CMIP5 MME also underestimates its amplitude (Figure 2d). The CMIP5 MME has the capacity to reproduce the patterns of the SAH in climatology. Thus, the CMIP5 MME can be used to analyze the responses of the SAH during different RF scenarios.

3. The Change of the SAH in RF Increasing and Stabilizing

The SAH responses show large differentiations in RF increasing and stabilizing scenario. When RF increasing, at 100 hPa, anomalous negative vorticity exists in the southern and central parts of climatological position of the SAH (black contour); anomalous positive vorticity resides in the northern region; and exceeding 80% models have consistent signs (Figure 3a). At 200 hPa, the SAH response exhibits anomalous positive vorticity in the northern region of the SAH, similar to the pattern at 100 hPa, but in its southern region, it displays anomalous positive vorticity, which is opposite to the response at 100 hPa (Figure 3c). The response is insignificant, and the model consistency is poor. During RF stabilization, at 100 hPa, it displays anomalous negative vorticity south of the climatological position of the SAH and anomalous positive vorticity north of the position (Figure 3b). Both patterns at 100 and 200 hPa resemble those during RF increase, but amplitudes are smaller (Figure 3). The opposite responses at different altitudes in south of the SAH are probably due to the potential temperature anomaly, θ', whose maximum is between 150 and 200 hPa (Qu et al., 2022). Reverse vertical temperature advection transported by climatological vertical motion, $\overline{\omega}\frac{\partial \theta'}{\partial p}$, at different altitudes leads to opposite changes in vertical

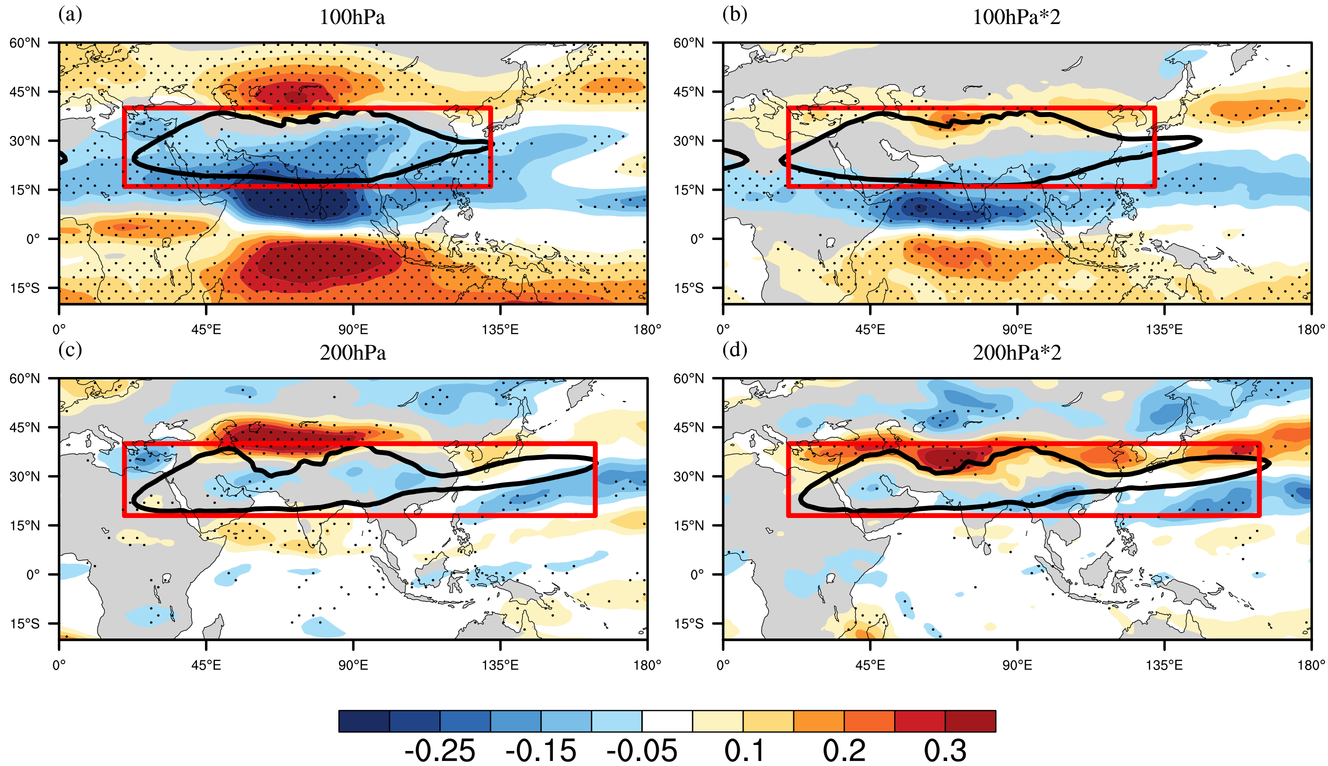

Figure 3. The responses of vorticity (units: $1 \times 10^{-5}\ s^{-1}$; color shading) and their climatology (units: $1 \times 10^{-5}\ s^{-1}$; black contour) over East Asia when radiative forcing (RF) increasing (a, c) and during RF stabilizing (b, d). In order to unify the color scale, the results during RF stabilization are scaled by 2. The results at 100 hPa are displayed in (a, b), and (c, d) are the results at 200 hPa. Coupled Model Intercomparison Project Phase 5 multimodel ensembles (MME) results are shown. The climatological vorticity of the South Asian High (SAH) is chosen to be $-1.2 \times 10^{-5}\ s^{-1}$ at 100 hPa and $-1.4 \times 10^{-5}\ s^{-1}$ at 200 hPa based on their performances in Figure 2. Stippling represents exceeding 80% of the model signs (10 out of 13) are consistent with MME. Red boxes are used for calculating the SAH strength index.

motion ω' over the SAH surrounding area. The reverse sign of the vertical velocity with pressure, $\frac{\partial \omega'}{\partial p}$, may cause distinct vorticity forcing and generate zonal vorticity advection to influence the SAH response over East Asia. As the mechanism at 200 hPa shares features with that at 100 hPa, changes at 100 hPa are mainly focused. The SAH expands southward at 100 hPa in both RF increasing and stabilizing, strengthens in RF increasing while changes little in RF stabilization (Figures 3a and 3b).

A linearized diagnostic equation of the vorticity budget at 100 hPa is adopted based on Equation 1 in Section 2.3. During RF increase, there is positive vorticity advection ($-\overline{\overline{V}} \cdot \nabla \zeta'$) in the Tibetan Plateau and northern IO and negative advection over the southern Arabian Peninsula (Figure 4b). The change in vorticity advection is mainly balanced by $f\frac{\partial \omega'}{\partial p}$, which is negative in northern IO and positive in Arabian Peninsula (Figure 4a). Over the northern IO and Tibetan Plateau, the vertical velocity decreases with pressure. The SAH enhances and moves equatorward during RF increase to balance the effect of the vertical velocity. During RF stabilization, vertical velocity increases with pressure over the SAH in climatology (black box in Figure 4e), leading the vorticity to evolve, the SAH reduces to balance this vorticity response.

To measure the SAH strength more precisely, a strength index is defined as the regional mean vorticity in the domain of 16–40°N, 20–132°E with latitudinal weights at 100 hPa. The domain is shown as red boxes in Figures 3a and 3b and covers the whole region of SAH climatology. The definition of the strength index at 200 hPa is the same as that at 100 hPa, except that the domain is 18–40°N, 20–164°E (shown as the red boxes in Figures 3c and 3d). During RF increase, the SAH enhances at 100 hPa but changes little at 200 hPa (Figure 5). During RF stabilization, the SAH changes little at 100 hPa and weakens at 200 hPa (Figure 5). The changes in SAH strength depend on pressure levels during RF increase and stabilization. Its response exceeds the 95% significance level at 100 hPa between RF increase and stabilization but is insignificant at 200 hPa. The SAH apparently strengthens at 100 hPa during RF increase but changes little during RF stabilizing.

10.1029/2023JD038616

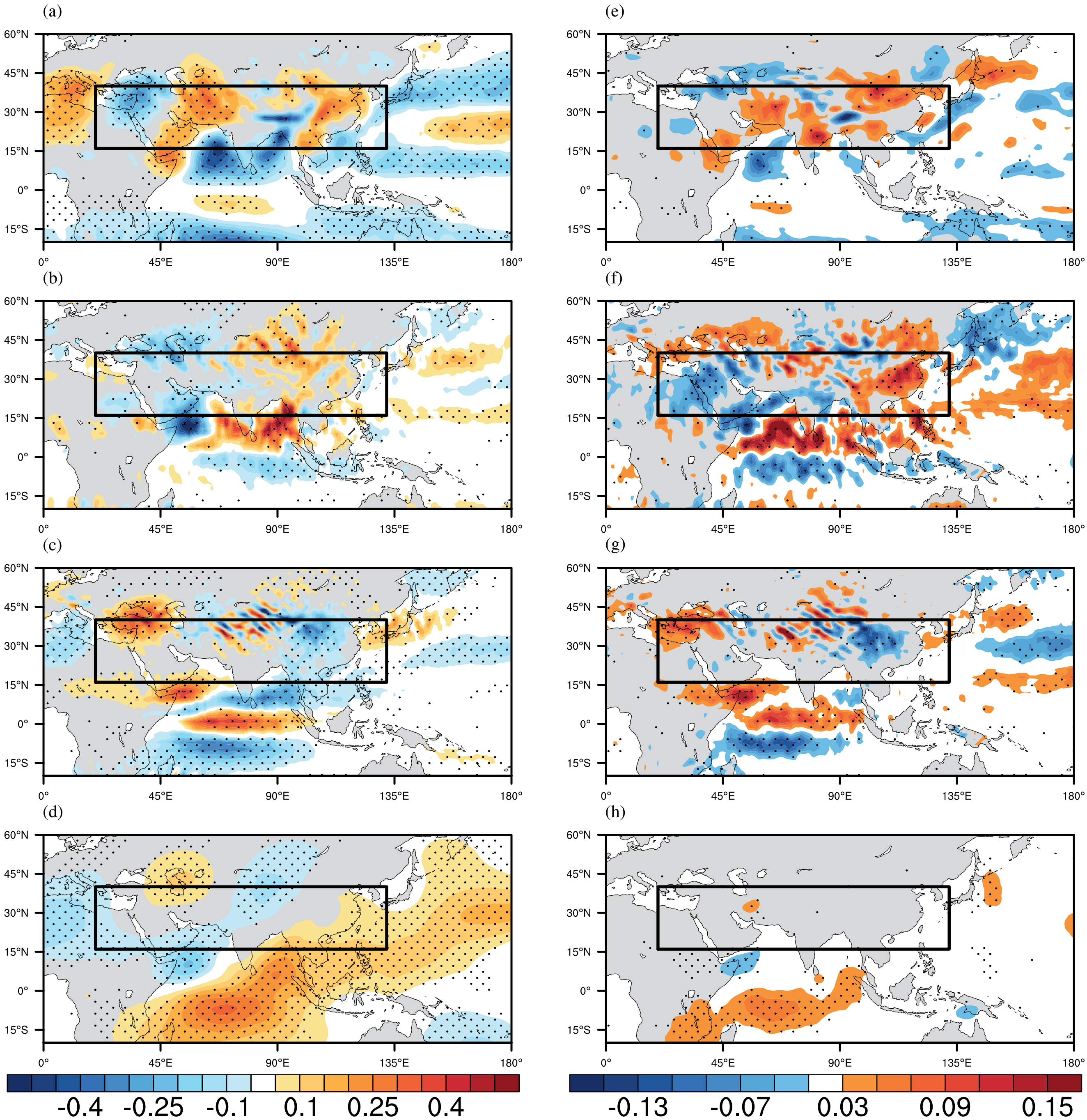

Figure 4. Distributions of the terms of the diagnostic vorticity equation (units: $1 \times 10^{-10}\ \mathrm{s}^{-2}$; shading) when radiative forcing (RF) increasing (a)–(d) and during RF stabilizing (e)–(h) at 100 hPa. The vorticity equation includes the gradients of vertical velocity change $f\frac{\partial \omega'}{\partial p}$ (a, e), horizontal advection of relative vorticity change $-\overline{\vec{V}} \cdot \nabla\zeta'$ (b, f), horizontal advection of relative vorticity in climatology $-\vec{V}' \cdot \nabla\overline{\zeta}$ (c, g), and geostrophic vorticity advection $-\beta v'$ (d, h). The black boxes are the same as the red boxes in Figure 3.

The location of the SAH zonal ridge can represent the longitudinal movement of the SAH. The SAH expands southward during RF increase and stabilization at both 100 and 200 hPa (Figure 6a) but is more significant at 100 hPa than at 200 hPa. The SAH meridional ridge moves westward at 100 hPa when RF increases; during RF stabilization, it shifts eastward at 100 and 200 hPa, but the shift is insignificant (not shown). Thus, the SAH has a significant southern expansion at 100 hPa in RF increasing and stabilizing scenario. Next section explores possible mechanisms of the strength and position responses of the SAH.

10.1029/2023JD038616

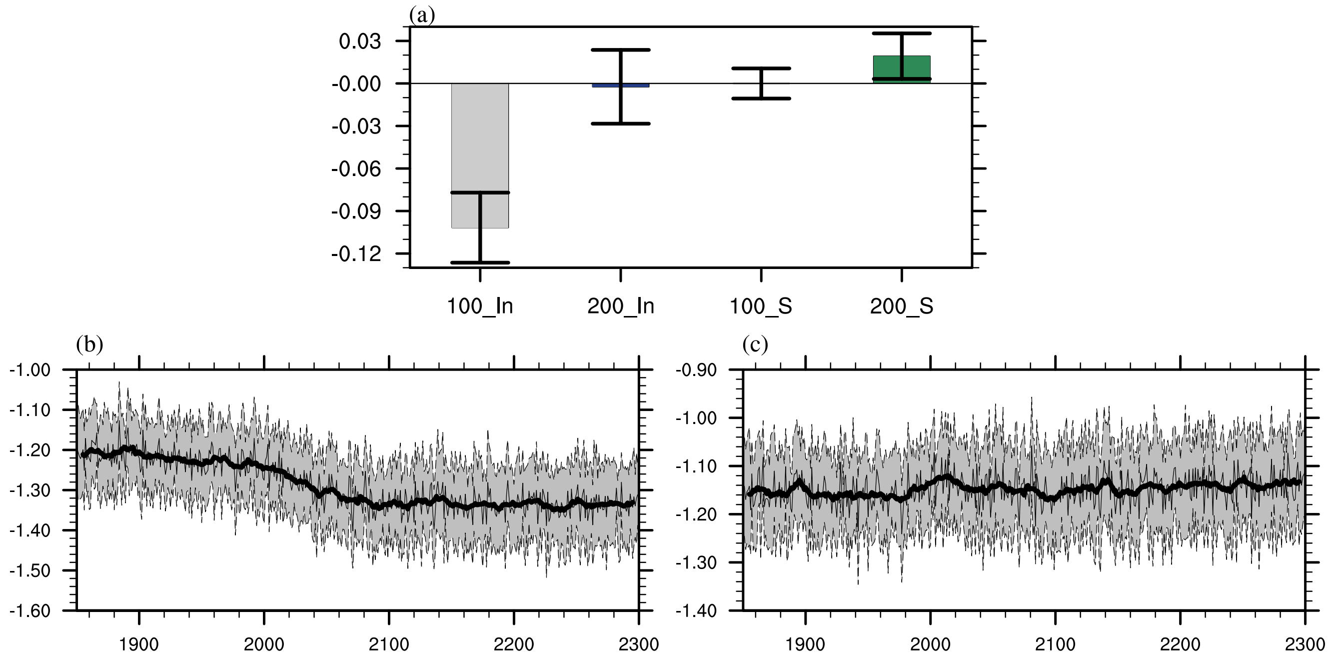

Figure 5. The South Asian High strength responses (a) and its evolution at 100 hPa (b) and 200 hPa (c) in increased and stabilizing radiative forcing (RF) scenario. The responses in RF increasing are shown as "In," and the responses during RF stabilization are shown as "S." According to the definition in Section 2.1, the "100_In" is the response at 100 hPa during RF increasing, the others are similar. The definition of the strength index at 100 hPa is the regional average over the domain (16–40°N, 20–132°E), and the index at 200 hPa is the mean over the region of 18–40°N, 20–164°E as shown by the red boxes in Figure 3. The color boxes are the Coupled Model Intercomparison Project Phase 5 (CMIP5) multimodel ensembles (MME) results, the error bar in (a) and shadows in (b, c) represent one standard deviation of intermodel variability relative to the MME results, and black lines in (b, c) are the CMIP5 MME results with an 11-year running average.

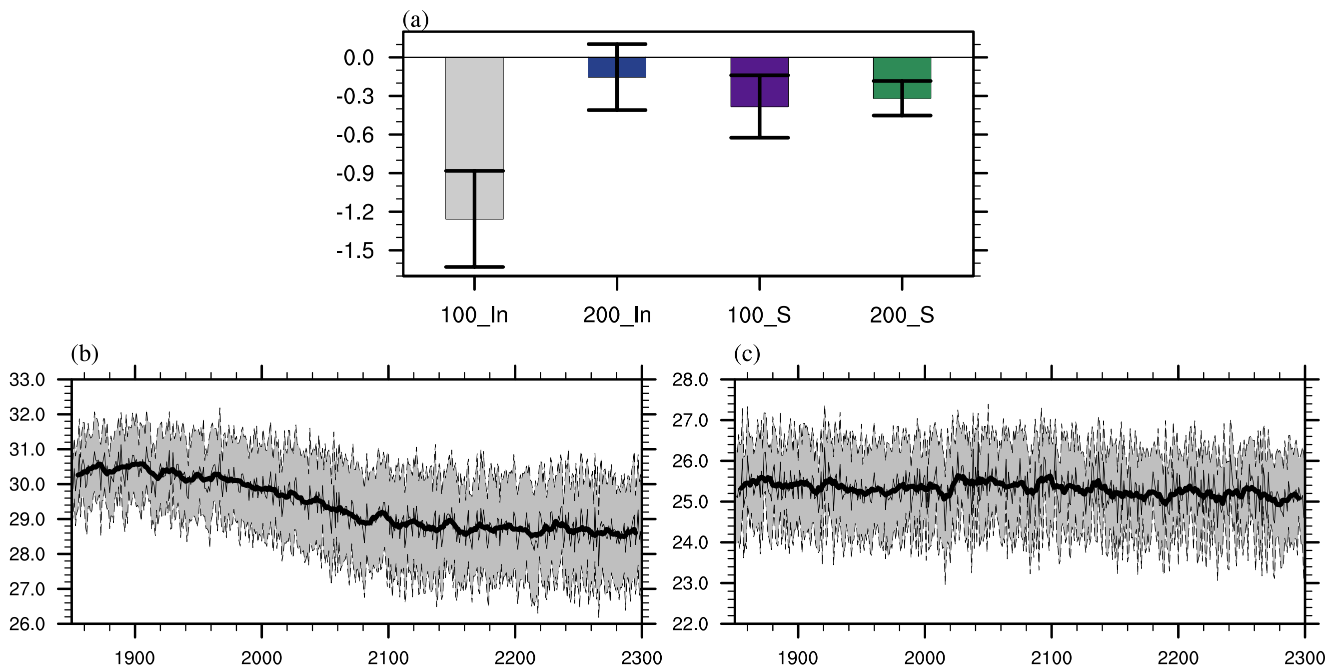

Figure 6. As Figure 5, but the changes of the latitude of the South Asian High zonal ridge.

4. The Influence of Heating on the SAH Responses

4.1. Diagnostic Equation

Heating may affect responses of atmospheric circulation (Gill, 1980; Qu & Huang, 2016). In theory, a prescribed heat source may induce local upward motion. Because the potential temperature in the atmosphere increases with altitude, the anomalous upward exists as a balance by bringing the cooler air parcel from the lower atmosphere to the higher one. Near the heat source, there is an anomalous anticyclone in higher atmosphere and an anomalous cyclone in lower atmosphere. A diagnostic equation (Equation 2) is employed to study circulation changes of heating. The regional climate responses are mainly influenced by three terms on right side of Equation 2: the mean advection of stratification change (*MASC*), the latent heating (LH^*), and residual (Re^*). Sum of the last two is the apparent heat source (Q_1^*), which is diabatic heating, and *MASC* is adiabatic heating associated with atmospheric stratification change. Homogeneous ocean heating influences atmosphere stratification (*MASC*) as the "wet-get-drier" mechanism, and the inhomogeneous warming of the ocean causes anomalous upward and downward motion in the atmosphere (Q_1^*) due to the "warmer-get-wetter" theory (Hou et al., 2021; Xie et al., 2010). Consideration about these two effects may lead to a comprehensive understanding of the atmospheric response (Hou et al., 2021; Qu & Huang, 2016). For example, under global warming, if *MASC* is taken into account, the atmospheric circulation slowdown is well reproduced by the model (Hou et al., 2021; Ma et al., 2018). These three terms are used to force the LBM to study the SAH changes in RF increasing and stabilizing scenario.

First, distributions of the three terms mass integrations from 1,000 to 100 hPa are displayed in Figure 7. During RF increase (Figures 7a–7c), LH^* displays heating over the northern tropical IO, southwestern region of China, North Pacific and intertropical convergence zone (ITCZ) and cooling in the North Atlantic and Southern Hemisphere (Figure 7a). Amplitude of LH^* is almost four times that of *MASC* (Figures 7a and 7b; Qu & Huang, 2016). *MASC* displays heating in the east coast of the Pacific and Atlantic and Southern Hemisphere and cooling in the northern IO and ITCZ (Figure 7b). Re^* is smaller than the other two (Figure 7c).

During RF stabilization, the amplitudes of the three terms are smaller than those during RF increase. LH^* displays a distinct pattern. There is cooling in the Maritime Continent, Indian Peninsula, northeastern tropical Pacific and southwestern Pacific, while heating over the southwestern tropical IO, North Pacific and South Pacific (Figure 7d). *MASC* is similar to that during RF increases, it also has an amplitude of about a quarter of LH^* (Figure 7e). *MASC* is determined by the global average warming and the climatology vertical velocity. The $\overline{\omega}$ pattern resembles the RF increase and stabilization. Because the warming rate is smaller during RF stabilization, smaller amplitude of *MASC* is due to the smaller $\langle \theta' \rangle$. Similar to that in the RF increase, Re^* distribution is more disperse than the other two (Figure 7f).

MASC patterns are different in the upper and lower troposphere. It displays cooling over the ITCZ below 300 hPa (Figures S1a–S1c in Supporting Information S1), similar to its mass integration results from 1,000 to 100 hPa. It is totally reversed above 300 hPa, heating over the ITCZ while cooling in the east coast of the Pacific and Atlantic and Southern Hemisphere (Figures S1d–S1f in Supporting Information S1). These opposite patterns between the higher layer and lower layer are due to the $\langle \theta' \rangle$ reaching a maximum at 300 hPa, which causes different signs of *MASC*. LH^* patterns resemble different altitudes, with its maximum in the mid-troposphere during RF increase and stabilization (Qu & Huang, 2016). Next, roles of the three-term heating in SAH responses are analyzed by forcing the LBM with their spatial global distribution in RF increasing and stabilizing.

4.2. Total Effects of Heating on SAH Responses

Heating can affect the atmosphere circulation responses through three components according to Equation 2: LH^*, *MASC* and Re^*. During RF increase, at 100 hPa, the LBM simulation forced by LH^* displays anomalous negative vorticity over East Asia and the Tibetan Plateau and positive vorticity in Central Asia (Figure S2a in Supporting Information S1). The amplitude of LBM simulation is almost the same as those of the CMIP5 MME results, but its negative center is more northerly than the CMIP5 result (Figure 3a and Figure S2a in Supporting Information S1). The simulation forced by *MASC* shows anomalous positive vorticity over East Asia and negative vorticity in the northern IO (Figure S2b in Supporting Information S1). The amplitude of the simulation forced by *MASC* is less than the CMIP5 result (Figure 3a and Figure S2a in Supporting Information S1). The simulation forced by Re^* shows anomalous negative vorticity over East Asia and the Tibetan Plateau, similar to the LH^* results (Figures S2a and S2c in Supporting Information S1).

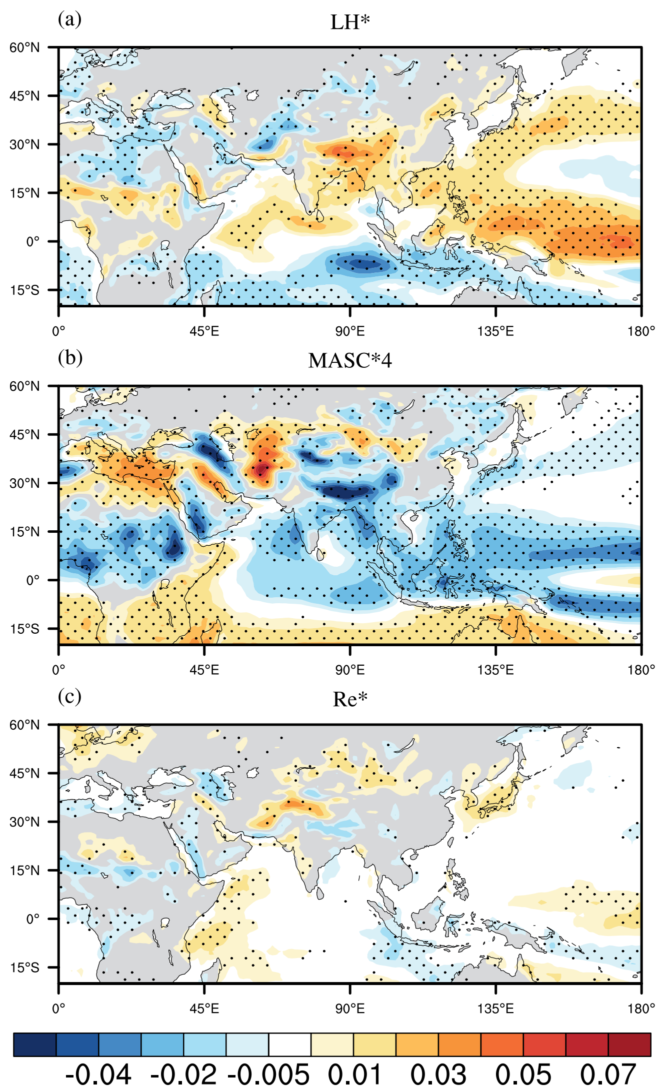

Figure 7. The horizontal patterns of mass integration of latent heating (*LH**; a, d), the mean advection of stratification (*MASC*; b, e) and residual term (*Re**; c, f) from 1,000 to 100 hPa during radiative forcing (RF) increase and stabilization (shading; units: K kg s^{-1} m^{-2}). The results of RF increasing are shown in left panels, results during RF stabilizing are shown in right panels. Coupled Model Intercomparison Project Phase 5 multimodel ensembles (MME) results are shown. Stippling represents exceeding 80% model signs (10 out of 13) are consistent with MME.

As mentioned in Section 2.4, *LH** and *Re** are two components of Q_1^* (diabatic heating). During RF increase, the roles of *LH** and *Re** are consistent; both show anomalous negative vorticity over the East Asia, which contribute to equatorward movement and strengthening of the SAH (Figure S2e in Supporting Information S1). The result forced by the three terms shows that anomalous negative vorticity exists over East Asia and the northern IO (Figure S2g in Supporting Information S1); it is alike with the SAH change pattern in CMIP5, but its negative center moves northward (Figure 3a and Figure S2g in Supporting Information S1). In general, during RF increase, *LH** and *Re** lead the SAH to strengthen, and the roles of the three terms, *LH**, *MASC* and *Re**, contribute to the SAH moving equatorward.

During RF stabilization, the LBM simulation forced by *LH** shows that anomalous negative vorticity exists over East Asia at 100 hPa (Figure 8a), alike with pattern in RF increasing (Figure S2a in Supporting Information S1). Negative center is further northward than CMIP5 MME result, which exists in the northern IO (Figure 3b). Simulation of *MASC* forcing is similar to that during RF increase; there is anomalous negative vorticity in the northern IO and positive vorticity in East Asia (Figure 8b and Figure S2b in Supporting Information S1). Similarly, the amplitude is smaller than the CMIP5 MME results (Figures 3b and 8b). The simulation forced by *Re** is

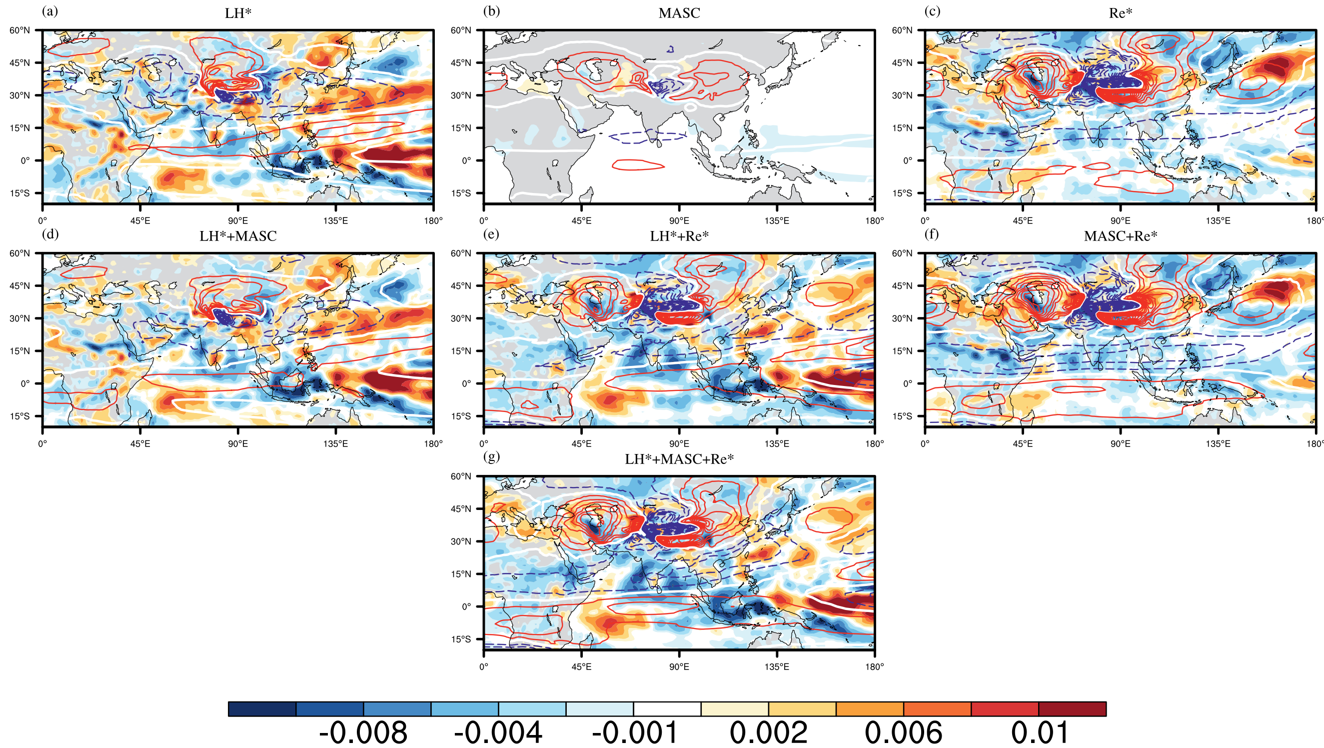

Figure 8. Vorticity responses (contours, contour interval: 0.016 s^{-1}; units: 1×10^{-5} s^{-1}) at 100 hPa of *MASC*, *Re** and *LH** forcing in the linear baroclinic model during radiative forcing stabilization. The simulation results forced by their combination and summation are also shown, and the relevant information is at the top of each figure. The heating pattern is in shading (units: K kg s^{-1} m^{-2}).

slightly distinct from that during RF increase; it displays anomalous positive vorticity over East Asia (Figure 8c), which is totally opposite to the CMIP5 MME (Figure 3b). During RF stabilizing, the simulations of *LH** and *Re** forcing are canceled out, leading to anomalous negative vorticity in the Indo-China Peninsula and positive vorticity in East Asia (Figure 8e), which reduces the SAH intensity but contributes its equatorward. The result of *LH** + *MASC* is slightly different from the result of the three terms: the result forced by the three terms shows anomalous positive over East Asia and negative vorticity in the northern IO (Figure 8g), but anomalous negative vorticity is northward in the simulation forced by *LH** + *MASC* (Figure 8d). Total heating is important in simulating the SAH response during RF stabilization, and *LH** + *MASC* play a more significant role among them. The role of *Re** cannot be ignored which may reduce SAH intensity.

During RF stabilization, SAH expands southward, but its strength changes little. The SAH location may be mainly due to the influences of *LH** and *MASC*. The roles of *LH** and *Re** are canceled out, leading to little change in SAH intensity. As mentioned in Section 2.4, Q_1^* includes *LH** and *Re**. In the next section, the roles of *MASC* (adiabatic heating) and Q_1^* (diabatic heating) in the SAH responses are studied.

4.3. Individual Effect of Apparent Heating and the Mean Advection of Stratification Change on SAH

The apparent heating pattern in the CMIP5 MME is used to force the LBM to study the influence of Q_1^* on the SAH responses. The mass integrations of Q_1^* patterns are different during RF increase and stabilization from 1,000 to 100 hPa (Figure 9). During RF increase, Q_1^* displays cooling in the North Atlantic and Southern Hemisphere but heating over northern tropical IO, the southwestern region of China, the ITCZ and the North Pacific, similar to *LH** pattern (Figures 7a and 9a). The simulations of the LBM forced by Q_1^* show that anomalous negative vorticity at 100 hPa exists over East Asia due to heating over the southwestern region of China and equatorial western Pacific (Figures S3c and S3d in Supporting Information S1). The simulation of heating forcing in the equatorial western Pacific also displays anomalous negative vorticity in the northern IO (Figure S3d in Supporting Information S1). Both of them indicate that the SAH has an obvious southern expansion and strengthening. The circulation responses are similar to those of the other two simulations (Figures S3a and S3b in Supporting

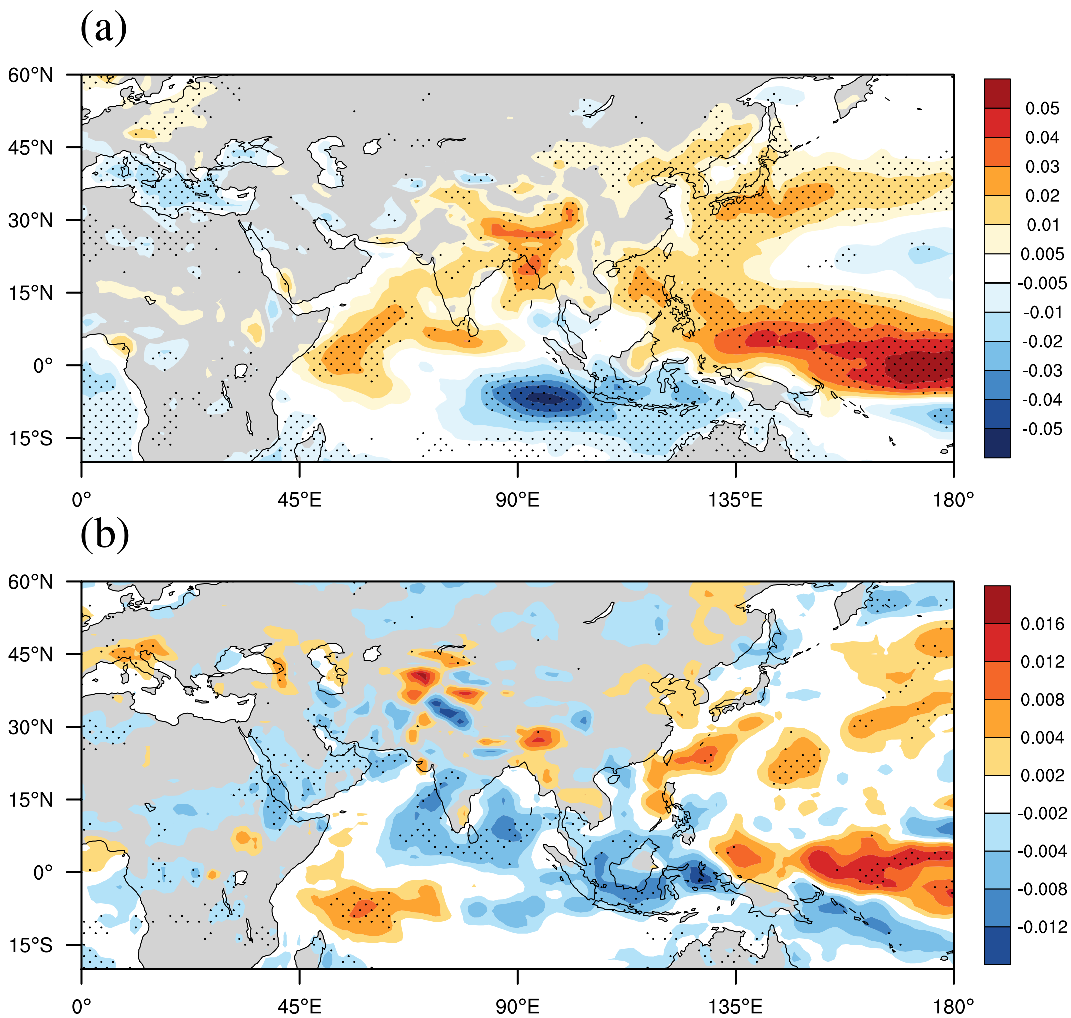

Figure 9. Mass integration of the apparent heat source (Q_1^*) patterns in radiative forcing increase (a) and stabilization (b) from 1,000 to 100 hPa (shading; units: K kg s^{-1} m^{-2}). Coupled Model Intercomparison Project Phase 5 multimodel ensembles (MME) results are shown. Stippling represents exceeding 80% model signs (10 out of 13) are consistent with MME.

Information S1). These conclusions are alike with Qu et al. (2015), although they analyzed simulation results forced by the *LH*. This may be due to the coincident role of *LH** and *Re** during RF increase (Figures S2a and S2c in Supporting Information S1). The simulations of the LBM forced by *Re** during RF increase are also performed (Figure S4 in Supporting Information S1). It shows that during RF increase, anomalous negative vorticity over the East Asia is mainly forced by the heating over the Asia continent (Figure S4a in Supporting Information S1), and the negative vorticity over the northern IO is mainly due to the heating over the central Pacific Ocean (Figure S4d in Supporting Information S1). *Re** and *LH** strengthen SAH and induce the SAH to move equatorward.

However, during RF stabilizing, Q_1^* pattern is totally different from that in the RF increase (Figure 9b). The amplitude is smaller than the former one. It displays cooling in the Maritime Continent, southwestern Pacific, northeastern tropical Pacific and Indian Peninsula but heating over the North Pacific, southwestern equatorial IO and South Pacific. The LBM simulations forced by Q_1^* show that the anomalous negative vorticity in the Indo-China Peninsula is mainly forced by heating over northern Pacific and tropical Pacific (Figures 10d and 10e). Anomalous positive vorticity over East Asia is mainly due to cooling over the Indian Peninsula and Maritime Continent (Figure 10c). The simulation forced by Q_1^* indicates that the SAH has a southern expansion during RF stabilization (Figure 10f). Because the roles of *LH** and *Re** are canceled out during RF stabilization, the simulations of the LBM forced by *Re** are also displayed (Figure S5 in Supporting Information S1). It shows that, during RF stabilization, the simulation forced by the anomalous cooling over the northern Pacific Ocean displays positive

10.1029/2023JD038616

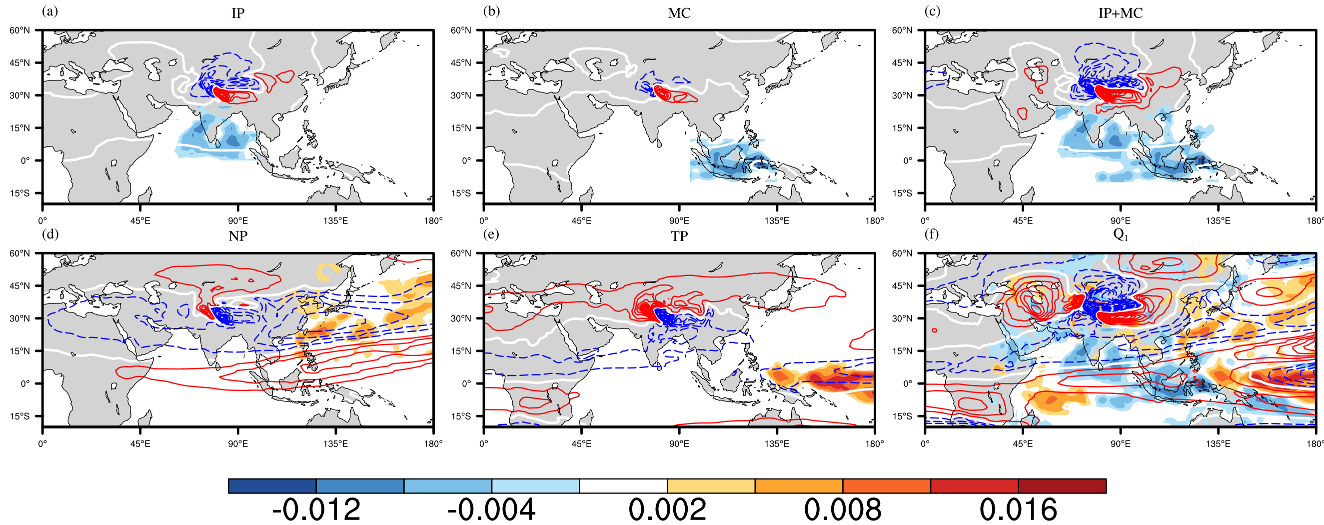

Figure 10. Vorticity responses (contours, contour interval: 0.01 s^{-1}; units: $1 \times 10^{-5}\ s^{-1}$) at 100 hPa in the linear baroclinic model forced by Q_1^* during radiative forcing stabilization. The heating pattern is in shading (units: K kg s^{-1} m^{-2}).

vorticity over the East Asia and negative vorticity over the South Asia (Figure S5b in Supporting Information S1). Besides, cooling over the Indian Peninsula also contributes to existing negative vorticity over the East Asia (Figure S5d in Supporting Information S1).

In addition to Q_1^*, *MASC* also plays a crucial role in SAH responses. Due to its opposite patterns at different pressure levels, *MASC* at lower levels (1,000–300 hPa) and upper levels (250–100 hPa) are used to force the LBM. The LBM simulations forced by *MASC* at different pressure levels differ widely. The simulations during RF stabilization are only focused on because of similar results. The LBM simulation forced by *MASC* in lower levels shows that there is anomalous positive vorticity over East Asia mainly due to cooling in ITCZ (Figures S6e and S6f in Supporting Information S1). However, *MASC* in upper levels excites anomalous negative vorticity over the northern IO mainly due to heating in the ITCZ (Figure S7d in Supporting Information S1). In conclusion, total role of *MASC* leads to the SAH moving equatorward (Figure 8b).

5. Model Spread of the SAH Change

Although the intermodel consistency in describing the changes of SAH during RF increase and stabilization well, model spread from the CMIP5 ensembles should also be discussed in the vorticity change. The intermodel empirical orthogonal function (EOF) analysis is adopted by analyzing the changes of vorticity at 100 hPa over the domain 10°S–60°N, 10–140°E during RF increase and stabilization, respectively. Before the EOF analysis, the intermodel standard deviation normalization of each grid is carried out.

During RF increase, the first mode of EOF accounts for 19.61% of the total variance. Figure 11b shows the normalized first principal component, and others in Figure 11 are the regression results of the vorticity at 100 hPa, the mass integration of *LH**, *MASC* and *Re** against the normalized principal component, respectively. The intermodel diversity of the vorticity change at 100 hPa shows significant negative vorticity over the East Asia and positive vorticity over the south Arabian Peninsula (Figure 11a). For *LH**, the model spread is related to the anomalous heating over the northwestern Pacific Ocean and ITCZ, and anomalous cooling over the northern IO and East Asia (Figure 11c). For *MASC*, the intermodel diversity is associated with the heating over the northern IO, eastern Pacific Ocean and south of the ITCZ, and cooling over the Maritime Continent and the northwestern Pacific Ocean (Figure 11d). For *Re**, it shows cooling over the northwestern Pacific Ocean and heating over the northern Pacific Ocean (Figure 11e). All of them are similar to the CMIP5 MME results (Figures 3 and 11c–11e).

For RF stabilization, the leading EOF accounts for 26.71% of the total variance. For vorticity, the intermodel diversity shows dipole structure over the East Asia, especially significant negative vorticity over the climatology of the SAH (Figure 12a). For *LH**, the model spread is associated with the heating over the northern Pacific

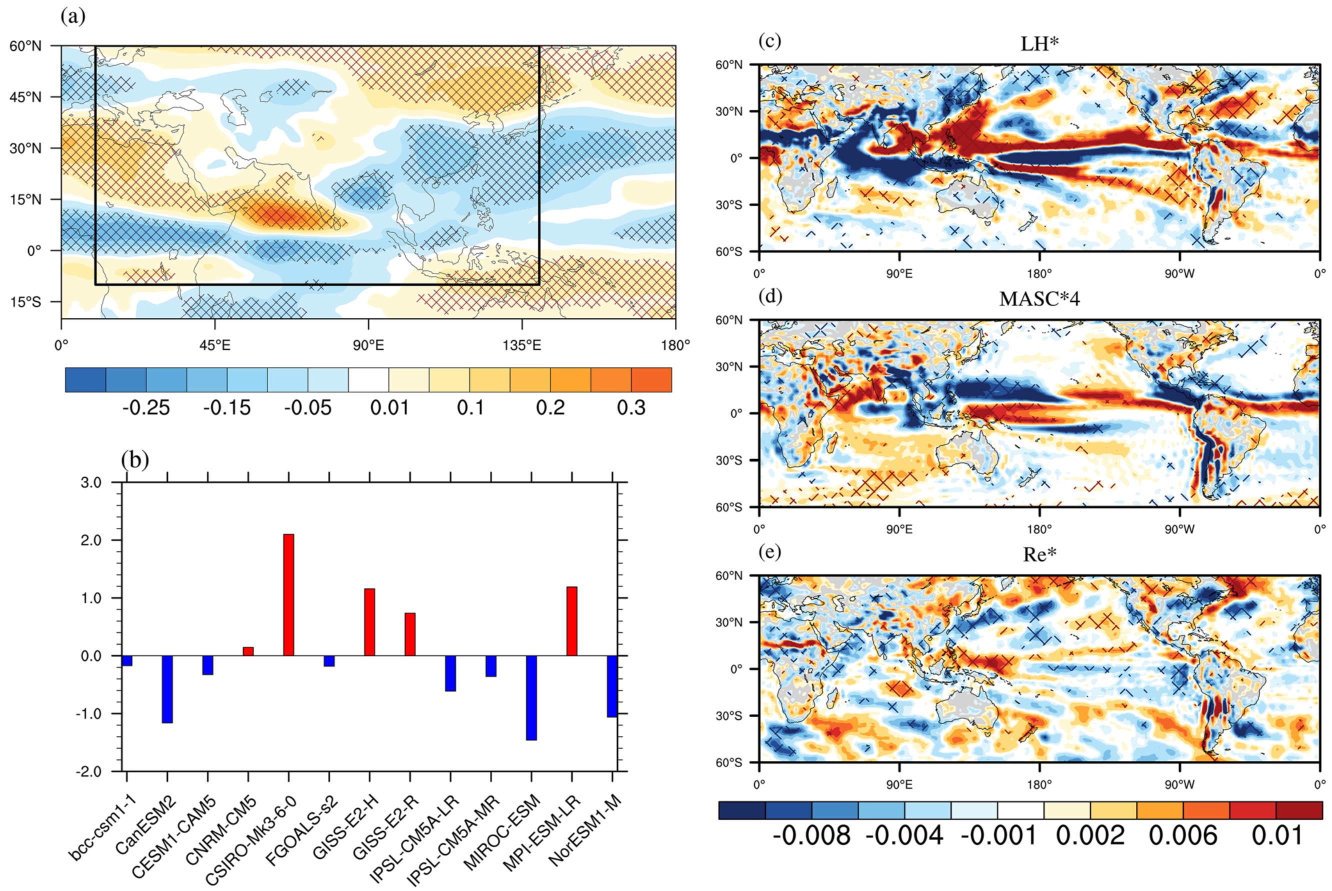

Figure 11. The regression results of the vorticity (a; color shading; units: s^{-1}) at 100 hPa, the mass integrations of the *LH** (c), *MASC* (d) and *Re** (e) against the normalized leading principal component (b) during radiative forcing increase. The units in (c)–(e) are K kg s^{-1} m^{-2}. The black box in (a) is the domain performing empirical orthogonal function, 10°S–60°N, 10–140°E. The red and blue lattice hatchings show the results reaching the 90% and −90% significance level, respectively.

Ocean and Indo-China Peninsula, cooling over the Maritime Continent and east coast over the Pacific Ocean (Figure 12c). For *MASC*, the intermodel diversity is related with the cooling over the northern IO and ITCZ, and heating over the southern IO and east coast of the Pacific and Atlantic Ocean (Figure 12d). This wider regression pattern is similar to the CMIP5 MME result, and it reaches the 90% significance. For *Re**, it shows anomalous cooling over the northwestern Pacific Ocean and heating over the northern and central Pacific Ocean (Figure 12e).

6. Summary

In this research, we investigated the SAH responses in RF increasing and stabilizing. At 100 hPa when RF increasing, the SAH intensifies and moves equatorward, while during RF stabilization, the SAH shifts equatorward with little intensity change. The number of models in the ECP4.5 experiment is slight small. Considering that the SAH is a large-scale climate system, and that there is a good intermodel consistency in the SAH responses during RF increase and stabilization, we think this limitation may not change the main conclusion of present manuscript. At 200 hPa, the SAH responses are not significant, and the model consistency is poor. These opposite responses at different altitudes south of the SAH are due to the change in potential temperature reaching a maximum at 150–200 hPa, which leads to opposite changes in vertical motion ω' over the SAH surrounding area to generate opposite zonal vorticity advection over East Asia. As the mechanism at 200 hPa shares features with that at 100 hPa, responses at 100 hPa are mainly focused.

To investigate the detailed processes leading to SAH changes, the present study divides the forcing into three terms: the mean advection of stratification change (*MASC*), the latent heating (*LH**) and residual heating

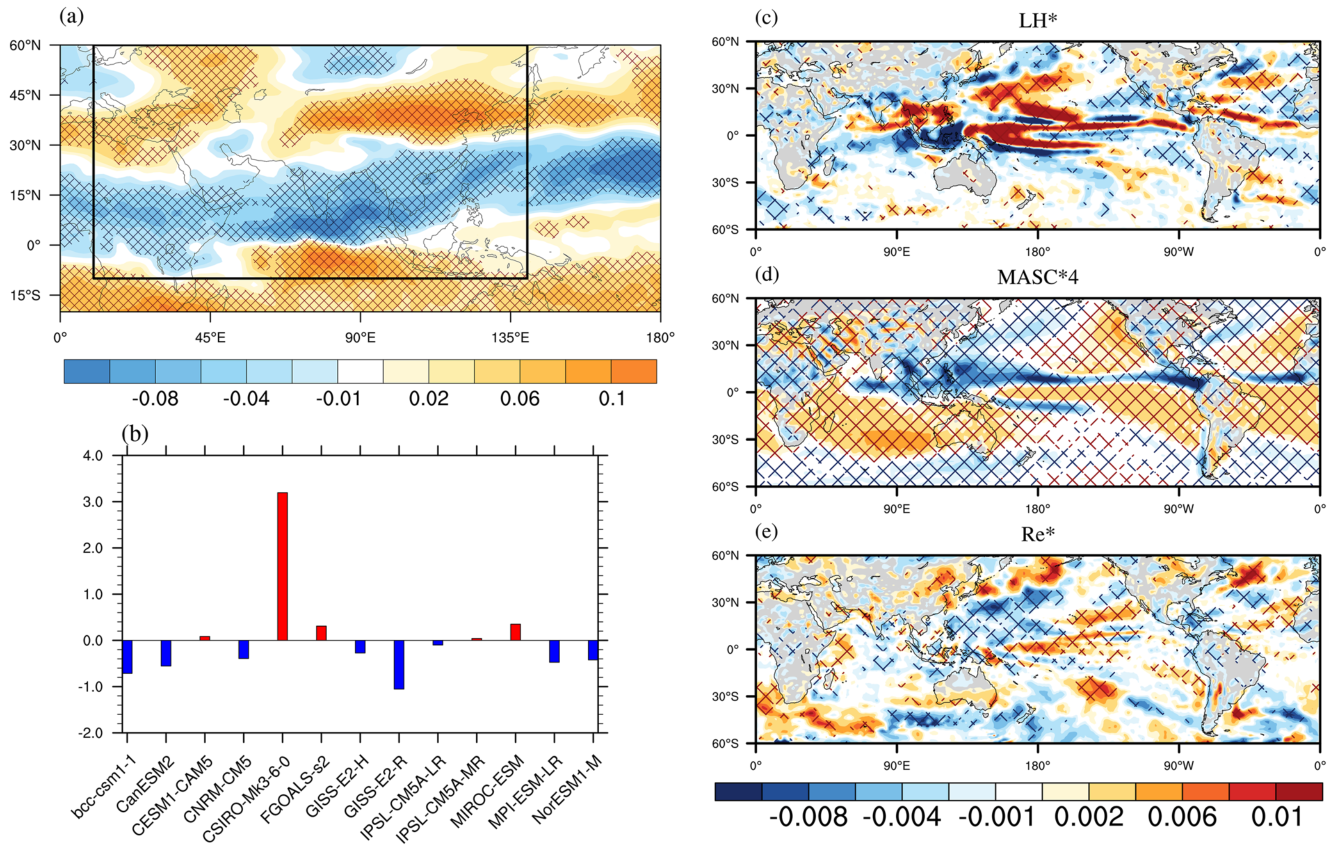

Figure 12. As for Figure 11, but for the results during radiative forcing stabilization.

(*Re**). The patterns of *LH** responses are different in RF increasing and stabilizing. In RF increasing, it displays heating in the southwestern region of China, northern tropical IO, ITCZ and the North Pacific and cooling in the North Atlantic and the Southern Hemisphere (Figure 7a); during RF stabilization, *LH** displays cooling over the northeastern tropical Pacific, Maritime Continent, southwestern Pacific and Indian Peninsula and heating in the North Pacific, southwestern tropical IO and South Pacific (Figure 7d). In RF increasing and stabilizing, *MASC* patterns are similar. Mass integration from 1,000 to 100 hPa exhibits cooling in the northern IO and ITCZ and heating in the east coast of the Pacific and Atlantic and Southern Hemisphere (Figures 7b and 7e). The vertical distributions of *MASC* are also similar between RF increase and stabilization; it displays anomalous cooling over the ITCZ below 300 hPa (Figures S1a–S1c in Supporting Information S1), similar to its mass integration results; the pattern is opposite above 300 hPa, showing heating over the ITCZ and cooling in the east coast of the Pacific and Atlantic and Southern Hemisphere (Figures S1d–S1f in Supporting Information S1). It is due to maximum $\langle \theta' \rangle$ at 300 hPa leads to opposite signs of *MASC* at different pressure levels.

Then, the global patterns of *LH**, *MASC* and *Re** are used to force the LBM to explore effects of the heating in RF increasing and stabilizing. In RF increasing, *LH** and *Re** contribute to SAH strengthening, and *LH**, *MASC* and *Re** lead to southward expansion of the SAH. During RF stabilization, *LH** and *MASC* contribute to the SAH moving equatorward; the roles of *LH** and *Re** cancel each other out, leading to little change in SAH intensity. The combination of the three terms is important in simulating the SAH response, and the role of *Re** cannot be ignored when RF stabilizing. Individual effects of *MASC* (as adiabatic heating) and Q_1^* (as diabatic heating, sum of *LH** and *Re**) are also analyzed. During RF stabilization, the SAH moving equatorward is major influenced by *MASC* in the upper troposphere (Figure S7d in Supporting Information S1) and Q_1^* over the northern Pacific and tropical Pacific (Figures 10d and 10e). Heating may influence the change of atmospheric circulation; in turn, the changes in the position and intensity of the SAH also leads to change in vertical velocity and affect the heating pattern. The interaction between the SAH and heating do exist which requires further study.

The *MASC* distribution due to global warming leads to a southward shift of the SAH. At the same time, the vertical change of the atmosphere with altitude in the tropics follows the wet adiabatic lapse rate, which decreases under global warming, resulting in the warming amplification in the upper troposphere of the tropics. The SAH is located in the upper troposphere of the Asian continent, near the tropics. Tropical warming amplification provides anomalous heating and moves the SAH southward. Therefore, under different climate mitigation strategies, we believe that with the increase of GMST, the warming amplification in the tropical upper troposphere and the *MASC*, may lead to the southward movement of SAH. But its intensity change is affected by various factors, and it is not very clear.

SAH shows consistent responses in RF increasing and stabilizing, despite different spatial patterns of *LH**. Rainfall-induced latent heating displays opposite distributions in RF along different paths due to deep ocean heat uptake (Hou et al., 2021). When RF stabilizing, deep ocean warming changes ocean stratification that slows ocean currents; it reduces the exchange of matter and energy between the shallow ocean and the deep ocean, leading to different sea surface temperature response patterns and affecting atmospheric circulation. Hence, deep ocean warming should not be ignored when examining the climate response during RF stabilization. The proposal of a carbon neutrality target also raises concerns about climate responses during RF stabilization. Our study reveals that deep ocean warming may influence the remote climate in East Asia and that climate responses during RF stabilization are unexpected. Our study also provides some new findings on global warming.

Data Availability Statement

Radiative forcing output is available from the RCP database website (https://tntcat.iiasa.ac.at/RcpDb/dsd?Action=htmlpage&page=compare; Smith & Wigley, 2006). The NCEP data are available online (https://psl.noaa.gov/data/gridded/data.ncep.reanalysis.derived.surface.html; Kalnay et al., 1996). The CMIP5 data sets are downloaded from the website https://esgf-data.dkrz.de/search/esgf-dkrz/. The LBM code is available online (https://ccsr.aori.u-tokyo.ac.jp/~lbm/sub/lbm_4.html; Watanabe & Kimoto, 2000). The related model simulations in LBM are available online at https://data.mendeley.com/datasets/c75nhyv2fn/2 (Hou et al., 2023).

Acknowledgments
The study was supported by the National Natural Science Foundation of China (42141019 and 42175055) and the Second Tibetan Plateau Scientific Expedition and Research (STEP) program (Grant 2019QZKK0102).

References

Bian, J. C., Li, D., Bai, Z. X., Li, Q., Lyu, D. R., & Zhou, X. J. (2020). Transport of Asian surface pollutants to the global stratosphere from the Tibetan Plateau region during the Asian summer monsoon. *National Science Review*, *7*(3), 516–533. https://doi.org/10.1093/nsr/nwaa005

Boos, W. R., & Kuang, Z. M. (2010). Dominant control of the South Asian monsoon by orographic insulation versus plateau heating. *Nature*, *463*(7278), 218–222. https://doi.org/10.1038/nature08707

Dickinson, R. E. (1981). Convergence rate and stability of ocean-atmosphere coupling schemes with a zero-dimensional climate model. *Journal of the Atmospheric Sciences*, *38*(10), 2112–2120. https://doi.org/10.1175/1520-0469(1981)038<2112:crasoo>2.0.co;2

Gill, A. E. (1980). Some simple solutions for heat-induced tropical circulation. *Quarterly Journal of the Royal Meteorological Society*, *106*(449), 447–462. https://doi.org/10.1256/smsqj.44904

He, C., Lin, A. L., Gu, D. J., Li, C. H., Zheng, B., Wu, B., & Zhou, T. J. (2016). Using eddy geopotential height to measure the western North Pacific subtropical high in a warming climate. *Theoretical and Applied Climatology*, *131*(1–2), 681–691. https://doi.org/10.1007/s00704-016-2001-9

Held, I. M., Winton, M., Takahashi, K., Delworth, T., Zeng, F. R., & Vallis, G. K. (2010). Probing the fast and slow components of global warming by returning abruptly to preindustrial forcing. *Journal of Climate*, *23*(9), 2418–2427. https://doi.org/10.1175/2009jcli3466.1

Hou, H. Y., Qu, X., & Huang, G. (2021). Reversal asymmetry of rainfall change over the Indian Ocean during the radiative forcing increase and stabilization. *Earth's Future*, *9*(10), e2021EF002272. https://doi.org/10.1029/2021EF002272

Hou, H. Y., Qu, X., & Huang, G. (2023). LBM-the South Asian High (Version 2) [Dataset]. Mendeley. https://doi.org/10.17632/c75nhyv2fn.2

Kalnay, E., Kanamitsu, M., Kistler, R., Collins, W., Deaven, D., Gandin, L., et al. (1996). The NCEP/NCAR 40-year reanalysis project [Dataset]. Bulletin of the American Meteorological Society, *77*(3), 437–471. https://doi.org/10.1175/1520-0477(1996)077<0437:TNYRP>2.0.CO;2

Kosaka, Y., & Nakamura, H. (2006). Structure and dynamics of the summertime Pacific–Japan teleconnection pattern. *Quarterly Journal of the Royal Meteorological Society*, *132*(619), 2009–2030. https://doi.org/10.1256/qj.05.204

Krishna, K. M. (2009). Intensifying tropical cyclones over the North Indian Ocean during summer monsoon-Global warming. *Global and Planetary Change*, *65*(1–2), 12–16. https://doi.org/10.1016/j.gloplacha.2008.10.007

Long, S. M., Xie, S. P., Du, Y., Liu, Q. Y., Zheng, X. T., Huang, G., et al. (2020). Effects of ocean slow response under low warming targets. *Journal of Climate*, *33*(2), 477–496. https://doi.org/10.1175/jcli-d-19-0213.1

Long, S. M., Xie, S. P., Liu, Q. Y., Zheng, X. T., Huang, G., Hu, K., & Du, Y. (2018). Slow ocean response and the 1.5 and 2°C warming targets. *Chinese Science Bulletin*, *63*(5–6), 558–570. https://doi.org/10.1360/n972017-01115

Long, S. M., Xie, S. P., Zheng, X. T., & Liu, Q. Y. (2014). Fast and slow response to global warming: Sea surface temperature and precipitation patterns. *Journal of Climate*, *27*(1), 285–299. https://doi.org/10.1175/JCLI-D-13-00297.1

Ma, J., Chadwick, R., Seo, K. H., Dong, C., Huang, G., Foltz, G. R., & Jiang, J. H. (2018). Responses of the tropical atmospheric circulation to climate change and connection to the hydrological cycle. *Annual Review of Earth and Planetary Sciences*, *46*(1), 549–580. https://doi.org/10.1146/annurev-earth-082517-010102

Ma, J., & Xie, S. P. (2013). Regional patterns of sea surface temperature change: A source of uncertainty in future projections of precipitation and atmospheric circulation. *Journal of Climate*, *26*(8), 2482–2501. https://doi.org/10.1175/jcli-d-12-00283.1

10.1029/2023JD038616

Ma, J., Xie, S. P., & Kosaka, Y. (2012). Mechanisms for tropical tropospheric circulation change in response to global warming. *Journal of Climate*, *25*(8), 2979–2994. https://doi.org/10.1175/jcli-d-11-00048.1

Manabe, S., Bryan, K., & Spelman, M. J. (1990). Transient response of a global ocean-atmosphere model to a doubling of atmospheric carbon dioxide. *Journal of Physical Oceanography*, *20*(5), 722–749. https://doi.org/10.1175/1520-0485(1990)020<0722:TROAGO>2.0.CO;2

Mason, R. B., & Anderson, C. E. (1963). The development and decay of the 100-mb summertime anticyclone over southern Asia. *Monthly Weather Review*, *91*(1), 3–12. https://doi.org/10.1175/1520-0493(1963)091<0003:TDADOT>2.3.CO;2

Qu, X., & Huang, G. (2016). The global warming–induced South Asian High change and its uncertainty. *Journal of Climate*, *29*(6), 2259–2273. https://doi.org/10.1175/jcli-d-15-0638.1

Qu, X., Huang, G., Hou, H. Y., Chen, Z. S., & Du, Y. (2022). The opposite response of the South Asian high to increasing CO_2 at different heights. *Atmospheric Science Letters*, *23*(8), e1093. https://doi.org/10.1002/asl.1093

Qu, X., Huang, G., Hu, K., Xie, S.-P., Du, Y., Zheng, X.-T., & Liu, L. (2015). Equatorward shift of the South Asian high in response to anthropogenic forcing. *Theoretical and Applied Climatology*, *119*(1–2), 113–122. https://doi.org/10.1007/s00704-014-1095-1

Rao, V. B., Ferreira, C. C., Franchito, S. H., & Ramakrishna, S. S. V. S. (2008). In a changing climate weakening tropical easterly jet induces more violent tropical storms over the North Indian Ocean. *Geophysical Research Letters*, *35*(15), L15710. https://doi.org/10.1029/2008GL034729

Sampe, T., & Xie, S. P. (2010). Large-scale dynamics of the Meiyu–Baiu rainband: Environmental forcing by the westerly jet. *Journal of Climate*, *23*(1), 113–134. https://doi.org/10.1175/2009JCLI3128.1

Sanderson, B. M., O'Neill, B. C., & Tebaldi, C. (2016). What would it take to achieve the Paris temperature targets? *Geophysical Research Letters*, *43*(13), 7133–7142. https://doi.org/10.1002/2016GL069563

Smith, S. J., & Wigley, T. M. L. (2006). Multi-gas forcing stabilization with Minicam [Dataset]. Energy Journal, *3*(01), 373–391. https://doi.org/10.5547/issn0195-6574-ej-volsi2006-nosi3-19

Sniderman, J. M. K., Brown, J. R., Woodhead, J. D., King, A. D., Gillett, N. P., Tokarska, K. B., et al. (2019). Southern Hemisphere subtropical drying as a transient response to warming. *Nature Climate Change*, *9*(3), 232–236. https://doi.org/10.1038/s41558-019-0397-9

von Schuckmann, K., Palmer, M. D., Trenberth, K. E., Cazenave, A., Chambers, D., Champollion, N., et al. (2016). An imperative to monitor earth's energy imbalance. *Nature Climate Change*, *6*(2), 138–144. https://doi.org/10.1038/nclimate2876

Wang, B., Jin, C. H., & Liu, J. (2020). Understanding future change of global monsoons projected by CMIP6 models. *Journal of Climate*, *33*(15), 6471–6489. https://doi.org/10.1175/JCLI-D-19-0993.1

Watanabe, M., & Kimoto, M. (2000). Atmosphere-ocean thermal coupling in the North Atlantic: A positive feedback [Software]. Quarterly Journal of the Royal Meteorological Society, *126*(570), 3343–3369. https://doi.org/10.1002/qj.49712657017

Wei, W., Zhang, R. H., Wen, M., Yang, S., & Li, W. H. (2019). Dynamic effect of the South Asian high on the interannual zonal extension of the western North Pacific subtropical high. *International Journal of Climatology*, *39*(14), 5367–5379. https://doi.org/10.1002/joc.6160

Wu, G. X., Liu, Y. M., He, B., Bao, Q., Duan, A. M., & Jin, F. F. (2012). Thermal controls on the Asian summer monsoon. *Scientific Reports*, *2*(1), 404. https://doi.org/10.1038/srep00404

Xie, S. P., Deser, C., Vecchi, G. A., Ma, J., Teng, H., & Wittenberg, A. T. (2010). Global warming pattern formation: Sea surface temperature and rainfall. *Journal of Climate*, *23*(4), 966–986. https://doi.org/10.1175/2009jcli3329.1

Yanai, M., Esbensen, S., & Chu, J. H. (1973). Determination of bulk properties of tropical cloud clusters from large-scale heat and moisture budgets. *Journal of the Atmospheric Sciences*, *30*(4), 611–627. https://doi.org/10.1175/1520-0469(1973)030<0611:dobpot>2.0.co;2

Zhang, L., Tang, C. G., Huang, J. P., Du, T., Guan, X., Tian, P. F., et al. (2021). Unexpected high absorption of atmospheric aerosols over a western Tibetan Plateau site in summer. *Journal of Geophysical Research: Atmospheres*, *126*(7), e2020JD033286. https://doi.org/10.1029/2020JD03328

Zhao, Y., Wang, M. Z., Huang, A. N., Li, H. J., Huo, W., & Yang, Q. (2014). Relationships between the West Asian subtropical westerly jet and summer precipitation in northern Xinjiang. *Theoretical and Applied Climatology*, *116*(3–4), 403–411. https://doi.org/10.1007/s00704-013-0948-3

Zheng, X. T., Hui, C., Xie, S. P., Cai, W. J., & Long, S. M. (2019). Intensification of El Niño rainfall variability over the tropical Pacific in the slow oceanic response to global warming. *Geophysical Research Letters*, *46*(4), 2253–2260. https://doi.org/10.1029/2018gl081414